

Bi-allelic Variations of SMO in Humans Cause a Broad Spectrum of Developmental Anomalies Due to Abnormal Hedgehog Signaling

Thuy-Linh Le, Yunia Sribudiani, Xiaomin Dong, Céline Huber, Chelsea Kois, Geneviève Baujat, Christopher T. Gordon, Valerie Mayne, Louise Galmiche, Valérie Serre, et al.

▶ **To cite this version:**

Thuy-Linh Le, Yunia Sribudiani, Xiaomin Dong, Céline Huber, Chelsea Kois, et al.. Bi-allelic Variations of SMO in Humans Cause a Broad Spectrum of Developmental Anomalies Due to Abnormal Hedgehog Signaling. American Journal of Human Genetics, 2020, 106, pp.779 - 792. 10.1016/j.ajhg.2020.04.010 . hal-03490735

HAL Id: hal-03490735
https://hal.science/hal-03490735

Submitted on 6 Jun 2022

HAL is a multi-disciplinary open access archive for the deposit and dissemination of scientific research documents, whether they are published or not. The documents may come from teaching and research institutions in France or abroad, or from public or private research centers.

L'archive ouverte pluridisciplinaire **HAL**, est destinée au dépôt et à la diffusion de documents scientifiques de niveau recherche, publiés ou non, émanant des établissements d'enseignement et de recherche français ou étrangers, des laboratoires publics ou privés.



Distributed under a Creative Commons Attribution - NonCommercial 4.0 International License

Version of Record: https://www.sciencedirect.com/science/article/pii/S0002929720301191
Manuscript_8258fcef2a527e1774c4f6d4e8e5e2bb

Biallelic variations of *SMO* in human cause a broad spectrum of developmental anomalies due to abnormal Hedgehog signaling.

Thuy-Linh Le,[1] Yunia Sribudiani,[2,3,20] Xiaomin Dong,[4,20] Céline Huber,[5] Chelsea Kois,[6] Geneviève Baujat,[5,7] Christopher T. Gordon,[1] Valerie Mayne,[8] Louise Galmiche,[9] Valérie Serre,[10] Nicolas Goudin,[11] Mohammed Zarhrate,[12] Christine Bole-Feysot,[12] Cécile Masson,[13] Patrick Nitschké,[13] Frans W. Verheijen,[2] Lynn Pais,[14] Anna Pelet,[1] Simon Sadedin,[4] John A. Pugh,[6] Natasha Shur,[15] Susan M White,[16] Salima El Chehadeh,[17] John Christodoulou,[4] Valérie Cormier-Daire, [5,7] RMW Hofstra,[2] Stanislas Lyonnet,[1,7] Tiong Yang Tan,[16] Tania Attié-Bitach,[7,18] Wilhelmina S. Kerstjens-Frederikse,[19] Jeanne Amiel,[1,7] Sophie Thomas,[1*]

[1]Université de Paris, *Imagine* Institute, Laboratory of Embryology and Genetics of Malformations, INSERM UMR 1163, F-75015 Paris, France.

[2]Department of Clinical Genetics, Erasmus Medical Center, 3015 GD Rotterdam, The Netherlands.

[3]Department of Biomedical Sciences, Division of Biochemistry and Molecular Biology, Faculty of Medicine, Universitas Padjadjaran, Bandung 40132, Indonesia.

[4]Brain and Mitochondrial Research Group, Murdoch Children's Research Institute, Royal Children's Hospital, 50 Flemington Rd, Parkville VIC 3052, Australia. Department of Paediatrics, University of Melbourne, Victoria 3010, Melbourne, Australia.

[5]Université de Paris, *Imagine* Institute, Laboratory of Molecular and Physiopathological Bases of Osteochondrodysplasia, INSERM UMR 1163, F-75015 Paris, France.

[6]Albany Medical Center, 43 New Scotland Ave, Albany, NY 12208, USA.

[7]Fédération de Génétique, Hôpital Necker-Enfants Malades, Assistance Publique Hôpitaux de Paris (AP-HP), 75015 Paris, France.

© 2020 published by Elsevier. This manuscript is made available under the CC BY NC user license
https://creativecommons.org/licenses/by-nc/4.0/

[8]Department of Medical Imaging, Royal Children's Hospital, Melbourne, Australia 3052.

[9]Department of Pathology, Hôpital Necker-Enfants Malades, Assistance Publique Hôpitaux de Paris (AP-HP), 75015 Paris, France.

[10]Université de Paris, Institut Jacques Monod, UMR7592 CNRS, 15 Rue Hélène Brion, 75013 Paris, France.

[11]Université de Paris, *Imagine* Institute, Cell Imaging, INSERM UMR 1163, F-75015, Paris, France.

[12]Université de Paris, *Imagine* Institute, Structure Fédérative de Recherche Necker, Genomic Platform, INSERM UMR 1163 & INSERM US24/CNRS UMS3633, F-75015, Paris, France.

[13]Université de Paris, *Imagine* Institute, Bioinformatics Platform, INSERM UMR 1163, F-75015, Paris, France.

[14]Center for Mendelian Genomics, Broad Institute of MIT and Harvard, 415 Main St, Cambridge, MA 02142, USA.

[15]Children's National, 111 Michigan Ave NW, Washington, D.C., 20010, USA.

[16] Victorian Clinical Genetics Services, Murdoch Children's Research Institute and Department of Paediatrics, University of Melbourne, Melbourne, Australia 3052.

[17]Service de Génétique Médicale, Hôpital de Hautepierre, 67098 STRASBOURG Cedex.

[18]Université de Paris, *Imagine* Institute, Laboratory of Genetics and Development of the Cerebral Cortex, INSERM UMR 1163, F-75015, Paris, France.

[19]Department of Genetics, University Medical Centre Groningen, Hanzeplein 1, 9713 GZ Groningen, The Netherlands.

[20]These authors contributed equally.

*Correspondence: sophie.thomas@inserm.fr

Abstract

The evolutionarily conserved Hedgehog (Hh) pathway is essential for organogenesis and plays critical roles in postnatal tissue maintenance and renewal. A unique feature of vertebrate Hh pathway is that signal transduction requires the primary cilium (PC) where major pathway components are dynamically enriched. These factors include Smoothened (SMO) and Patched, that constitute the core reception system for Sonic Hedgehog (SHH) as well as GLI transcription factors, the key mediators of the pathway. Here, we report biallelic loss-of-function variations in *SMO* in seven cases from five independent families causing a wide phenotypic spectrum of developmental anomalies affecting the brain (hypothalamic hamartoma, microcephaly), heart (atrioventricular septal defect), skeleton (postaxial polydactyly, narrow chest, shortening of long bones) and the enteric nervous system (aganglionosis). Affected individual-derived cells showed normal ciliogenesis but severely altered Hh-signal transduction due to either altered PC trafficking or abnormal activation of the pathway downstream of SMO. In addition, Hh-independent GLI2 accumulation at the PC tip in cells from the affected individuals suggests a potential function of SMO in regulating basal ciliary trafficking of GLI2 when the pathway is off. Thus, loss of SMO function results in abnormal PC dynamics of key components of the Hh signaling pathway and leads to a large continuum of malformations in humans.

Short Title: *SMO* mutations cause a broad spectrum of developmental anomalies due to abnormal Hedgehog signaling

Introduction

Hedgehog (Hh) signaling is a key evolutionarily conserved pathway during development and patterning of most organs. A unique feature of the vertebrate Hh pathway is that the primary cilium (PC) is critical for signal transduction [1]. PC is a microtubule-based organelle emanating from the surface of most cells [2], in which the components of the Hh pathway are enriched dynamically in response to Hh ligand. In the absence of Hh ligand, its receptor Patched 1 (PTCH1) localizes to the PC where it inhibits Smoothened (SMO), a second transmembrane protein belonging to the class F family of G-protein coupled receptors (GPCRs). Binding of Sonic Hedgehog (SHH) to PTCH1 leads to the exit of PTCH1 and the entry of SMO into the PC, where SMO activation culminates in GLI-dependent transcriptional activities [3,4]. In mammals, the GLI family consists of three members (GLI1, GLI2 and GLI3) that shift between activating (GLI^A) and repressive (GLI^R) forms to shape the Hh response. When the pathway is off, $GLI3^R$ is the predominant repressor of Hh target genes, whereas $GLI2^A$ is the predominant activator when the pathway is on [5].

In humans, deregulation of the Hh pathway leads to both malformations and cancers. Heterozygous germline mutations in *SHH* [MIM: 600725] and *PTCH1* [MIM: 300828] cause holoprosencephaly, while somatic or germline truncating *PTCH1* mutations can cause basal cell nevus syndrome (BCNS, [MIM: 109400]), also called Gorlin syndrome. Monoallelic germline variations in *SUFU* [MIM: 607035] can also cause BCNS while biallelic hypomorphic mutations can cause Joubert syndrome (JBTS, [MIM: 213300]). Biallelic *GLI1* [MIM: 165220] mutations lead to a phenotypic spectrum ranging from isolated postaxial polydactyly to a broader phenotype overlapping Ellis-van Creveld syndrome (EVC, [MIM: 225500]) [6]. Germline heterozygous truncating variants in *GLI2* [MIM: 165230] can cause Culler-Jones syndrome (CJS, [MIM: 615849]), associating postaxial polydactyly and hypopituitarism or holoprosencephaly (HPE9; [MIM: 610829]) [7,8]. Considering *GLI3* [MIM:

165240], germline heterozygous loss-of-function mutations are reported in Greig Cephalopolysyndactyly Syndrome (GCPS, [MIM: 175700]) and isolated polydactyly, while frameshift mutations located in the middle third of *GLI3* lead to constitutive $GLI3^R$ and cause Pallister-Hall syndrome (PHS, [MIM: 146510]). Finally, activating somatic missense mutations in *SMO* [MIM: 601500] are found in sporadic basal cell carcinoma (BCC, [MIM: 605462]), medulloblastoma and in Curry-Jones syndrome (CRJS, [MIM: 601707]) [8,9].

Here, we identified biallelic loss-of-function variations in *SMO* leading to severely altered Hh-signal transduction and causing pleiotropic developmental anomalies, affecting brain, heart, enteric nervous system (ENS) and skeletal development, with postaxial polydactyly as a consistent feature. *SMO* is thus a novel example of a key Hh pathway component for which loss-of-function and activating mutations can cause developmental disorders and cancer, respectively.

Materials and Methods

Affected individuals

Informed consent was obtained for all participating families, and the study was approved by the Ethical Committee of Paris Ile de France II. Family 2 was recruited via GeneMatcher [10].

Whole exome sequencing

Genomic DNA was extracted from peripheral blood samples. Briefly, Agilent SureSelect libraries were prepared from 3 µg of genomic DNA sheared with a Covaris S2 Ultrasonicator. Exome capture was performed with the 51 Mb SureSelect Human All Exon kit V5 (Agilent technologies) and sequencing was carried out using a HiSeq2500 (Illumina) machine. After demultiplexing, paired-end sequences were mapped on human genome reference (NCBI build37/hg19 version) using Burrows-Wheeler Aligner (Illumina). Downstream processing

was carried out with the Genome Analysis Toolkit (GATK), SAMtools, and Picard Tools, following documented best practices from the Broad Institute. An in-house software tool (PolyWeb) was used to annotate (based on Ensembl release 71) and filter variants according to relevant genetic models. We excluded known variants listed in the public databases dbSNP (build 135), the Exome Variant Server (release ESP6500SI-V2), the 1000 genomes variants (release date 21-05-2011) and variants previously identified in "in-house" exomes. Then we selected for variants affecting splice sites or coding regions (non-synonymous substitutions, insertions or deletions). Targeted resequencing was performed as described previously [11]. Sanger sequencing using the primers described in Table S2 was performed to validate the NGS findings and the segregation of the mutation within all the families.

Cell culture

Fibroblasts were obtained from skin biopsies of affected individuals and cultured in Optimem supplemented with 10% FBS, 100 U ml^{-1} penicillin and 100 mg ml^{-1} streptomycin (all from Life Technologies). Ciliogenesis was induced by starving the cells in serum-free Optimem for 24 h.

SHH pathway induction: recombinant human SHH (rhSHH), High Activity (R&D systems, 8908-SH, C-terminal cholesterol, N-terminal fatty acid-modified), 100ug/ml for 24h after 48h serum starvation; Smoothened Agonist, HCl (SAG, Santa Cruz sc-202814), 10 ug/ml for 24h after 48h serum starvation. cAMP/PKA activation/inhibition: Forskolin treatment for 1h (FSK, 1µM).

Reverse transcription quantitative Real Time PCR (RT-qrtPCR)

RNA was extracted from fibroblasts using RNeasy kit (QIAGEN) and first strand cDNA was synthesized using the GeneAmp RNA PCR Core Kit (Applied Biosystems) with random

hexamer primers. qrtPCR was carried out with the GoTaq qPCR master mix (Promega) in a Realplex 2 Mastercycler (Eppendorf), using *SMO*, *GLI1* and *PTCH1* primers and primers for two housekeeping genes *GUSB* and *HPRT* (Table S2). *SMO*, *GLI1* and *PTCH1* expression data performed in triplicate were normalized to *GUSB* and *HPRT* mRNA expression data. Data were analyzed with the $2^{-\Delta\Delta Ct}$ method Data are presented as relative levels ±SEM. **p<0.05; ***p<0.001 (Kolmogorov-Smirnov test).

Western blot

Protein was extracted from fibroblasts using RIPA buffer containing Protease Inhibitor Cocktail (Roche). 50mg of protein was separated by 10% SDS-PAGE and probed with rabbit anti-GLI3 AF3690 antibody (R&D Systems, 1:500) followed by HRP-conjugated secondary antibody and ECL-Prime detection (Amersham). An antibody against GAPDH (Abcam; ab9458) was used as a loading control. Densitometry using Bio-Rad Image Lab software was used to measure protein levels.

Immunofluorescent analysis

Fibroblasts were fixed in 4% PFA or in ice-cold methanol, permeabilized with 0.2% Triton-X 100 and incubated in 3% BSA, 0.1% Tween20 before incubation with primary antibodies at 4°C overnight followed by incubation with secondary antibodies for 30 min at room temperature. DNA was stained with DAPI. Confocal images were taken on a Zeiss LSM 700 microscope. Images were analyzed with ImageJ. All experiments were performed in triplicate with four fields acquired per condition, and an average of 15 cells per field. Cilia frequency was calculated by dividing PC counts by nuclei counts. PC length was measured after three-dimensional reconstruction of PC using Imaris software (Bitplane AG, Zurich, Switzerland), which allowed for length assessment irrespective of angle of orientation. To characterize

SMO and GLI2 trafficking to the PC, we measured the percentage of cells with SMO within the PC and those with an enrichment of GLI2 at the PC tip after SAG or rhSHH treatment. All antibodies are listed in Table S3.

Statistical analysis

Results are presented as means of at least *n*=3 independent experiments. Statistical analyses on pooled data were performed with the GraphPad Prism software by using Kruskal-Wallis, Kolmogorov-Smirnov or Fisher's exact tests.

Results

P1, a male, is the only child of non-consanguineous parents originating from France (F1-II:1). At birth, he presented with postaxial polydactyly of all four limbs, hypothalamic hamartoma, gelastic epilepsy and Hirschsprung disease (HSCR, [MIM: 142623]) (Figure 1, Table 1, Table S1). PHS was suspected and high throughput sequencing of a diagnostic panel of genes causing human ciliopathies or disorders of Hh-signal transduction including *GLI3* [MIM: 146510] identified no mutation. Whole exome sequencing (WES) in trio revealed two heterozygous variants in *SMO* (NM_005631.4): a missense (c.781C>T, p.(Arg261Cys)) and a nonsense (c.1339G>T, p.(Glu447*)) mutation, each inherited from one parent (Figure 2, Table 2). The nonsense variant falls in exon 7 of 12 total and is therefore presumed to lead to loss-of-function via nonsense-mediated mRNA decay (NMD). Accordingly, quantitative Real Time-PCR (qrtPCR) on mRNA extracted from fibroblasts from P1 showed *SMO* expression decreased to 50% compared to age-matched controls (Figure 3A) and subsequent cDNA sequencing confirmed that almost all remaining *SMO* mRNAs carried the missense allele (Figure 3B). 3D modeling of the active G_i-coupled hSMO crystal structure (PDB ID: 6OT0)

[12] showed that the Arg261 residue is located in the intracellular loop 1 (ICL1) that has been proposed to be crucial for SMO interaction with the $G\alpha_i$ protein, a direct downstream effector of SMO (Figures 3C and 3D) [13]. Structural comparison of active G_i-coupled hSMO and inactive hSMO (PDB ID: 5L7D) [14] showed different conformations of Arg261, suggesting its involvement in the activation of SMO (Figure 3E). In addition, the substitution of Arg to Cys at amino acid 261 is predicted to modify the distance of the hydrogen bond between this residue and the Tyr262 backbone (Figure 3F), potentially affecting the stability of the protein.

WES analysis of other individuals with a PHS-like phenotype without *GLI3* variants led to the identification of biallelic variants in *SMO* in two affected sibs in family F2 (F2-II:1 (P2) and F2-II:2 (P3)), inherited from their heterozygous parents. Both sibs presented with hypothalamic hamartoma, gelastic epilepsy and postaxial polydactyly. In addition, P2 had microcephaly (Figure 1, Table 1, Table S1) as previously reported [15]. The paternally inherited variant, c.2291_2292delAG, is located in the last exon of *SMO* and thus predicted to escape NMD and lead to a truncated protein, p.(Gln764Argfs*52). The maternally inherited variant was suspected by WES to be a deletion of at least 29 Kb encompassing exon 1 of *SMO* and exons 2-8 of *TSPAN33*. In an attempt to confirm the deletion and define the break points, we used targeted resequencing to capture a region of 153 Kb of genomic DNA from P2 covering the deleted interval (Figure 2). This analysis and subsequent Sanger sequencing with breakpoint-flanking primers, indicated that the deletion breakpoints are 62 Kb apart (chr7 g.128778292_128840690del), encompassing exon 1 of *SMO* and all exons of *TSPAN33* (Figure S1). Interestingly, both break points map to two short interspersed nuclear elements (SINEs) of the same Alu family; AluSx and AluSz repeats (Figure 2) suggesting non-homologous allelic recombination as the deletion mechanism. No *TSPAN33* variant was identified in the hemizygous allele of the affected sibs. RT-qrtPCR on mRNA extracted from fibroblasts of the siblings revealed a decrease of *SMO* mRNA level by 50% compared to

controls (Figure 3A). cDNA sequencing identified the mRNA harboring the 2bp deletion that had escaped NMD (Figure 3B), and is predicted to lead to a truncated protein lacking a part of the C-terminal cytoplasmic tail of SMO required for SMO ciliary accumulation and activation [16,17]. In particular, this highly evolutionary conserved region contains two serine residues (Ser771 and Ser785) corresponding to Ser777 and Ser791 in mouse Smo (mSmo) (Figure 3C, Figure S2), constituting two out of six phosphorylation sites essential for controlling SMO activation and ciliary localization[16].

We also identified *SMO* biallelic variants in four additional individuals from three families who had syndromic postaxial polydactyly. In family 3, the affected male (F3-II:1 or P4) had been diagnosed with Jeune asphyxiating thoracic dysplasia (JATD, [MIM: 208500]). He presented with bilateral, symmetrical sublingual soft tissue appendages, disproportionate short stature, short ribs, a trident appearance of the pelvis, short long bones and postaxial polydactyly of all four limbs (Figure 1, Table 1, Table S1). By trio WES, we identified that he was homozygous for a *SMO* variant (c.1285A>T; p.(Ile429Phe)), which was inherited from both of his parents. This variant is predicted *in silico* to be deleterious for the function of the protein (Table 2), but also to affect splicing by reinforcing a cryptic acceptor splice site located 26 bp downstream of the canonical one. Quantification of *SMO* mRNA level showed a decrease of 60% in the fibroblasts from P4 compared to control cells (Figure 3A). cDNA sequencing confirmed a partial splicing defect resulting in the skipping of the first 26 bp of exon 7 (Figure 3B), leading to a frameshift and a premature stop codon (p.(Gly422Glufs*9)). This abnormal transcript partially escapes NMD and may be translated to a truncated SMO protein lacking the TM5-6 and C-terminal tail and thus predicted to be unstable or inactive. Ile429, being located in the intracellular loop 3 (ICL3, Figures 3C and 3D), is involved in SMO interaction with the α5 helix of the $G\alpha_i$ protein required for SMO mediated signal transduction [12]. In family F4, the affected child (F4-II:4 or P5) presented with characteristic

features of EVC syndrome, another Short-rib thoracic dysplasia (SRTD), associating multiple gingival frenulae with dysplastic teeth (small, conical), complete atrioventricular septal defect (AVSD, [MIM: 606215]), postaxial polydactyly of the upper limbs with Y-shaped metaphysis, narrow chest and trident-shaped pelvis, but normal stature (Figure 1, Table 1, Table S1). Trio WES analysis led to the identification of *SMO* compound heterozygous variants affecting the same amino acid residue: c.1727G>A; p.(Arg576Gln) and c.1726C>T; p.(Arg576Trp)). Finally, a homozygous missense variant in *SMO* also involving Arg576 (c.1726C>T; p.(Arg576Trp)) was detected in a fifth family with two affected sibs (F5-II:2 (P6), F5-II:3 (P7)) born to consanguineous parents and presenting complete (P6) or partial (P7) AVSD and postaxial polydactyly of all four limbs (Figure 1, Table 1, Table S1). In fibroblasts from P6 and P7, the expression of *SMO* remained in the normal range compared to controls, indicating stability of the mutated mRNAs (Figure 3A), and sequencing of fibroblast-derived cDNA confirmed the presence of the variant (Figure 3B). All three missense variants reported here are predicted deleterious *in silico* by Polyphen2, SIFT and CADD (Table 2). Finally, Arg576 is located in the C-terminal cytoplasmic tail of SMO required for its activation as mutagenesis of the corresponding Arg580 in mSmo resulted in severe loss of mSmo activity [18].

To first analyze PC assembly in cells of individuals harboring biallelic *SMO* variants, we induced ciliogenesis by using serum starvation–mediated cell cycle arrest in confluent fibroblasts from five affected (P1-P4 and P6) and two control individuals (C1 and C2) and visualized PC by immunostaining with antibodies raised against acetylated alpha tubulin and pericentrin. We found normal PC number, size and shape in cells from all affected individuals compared to controls (Figures 4A, 4B and 4C). These results are in accordance with previous observations in animal models where Smo is not required for normal ciliogenesis. We next

tested the transduction of the Hh pathway in cells from P1-P4, P6 and P7 stimulated by addition of recombinant human SHH (rhSHH) or smoothened agonist (SAG), followed by quantification of the expression of two Hh target genes, *GLI1* and *PTCH1*. Compared to control cells, neither *GLI1* nor *PTCH1* expression were induced in cells from affected individuals, indicating a severe alteration of Hh pathway transduction (Figure 4D). These results suggest a loss-of-function mechanism of the identified *SMO* variants in the affected individuals.

We next analyzed SMO trafficking to the PC in cells derived from affected individuals in response to rhSHH stimulation. In control cells, SMO is enriched within the PC in response to rhSHH treatment. In cells from affected individuals, SMO is undetectable within the PC in three cases (P1, P2, P3) (Figures 4E and 4F), suggesting early destabilization or altered trafficking of mutated SMO, supporting the hypothesis of loss-of-function mechanism. In the remaining two (P4, P6), SMO is only partially translocated into the PC as the percentage of SMO positive PC appears significantly diminished as compared to controls. The transduction of the Hh signal remains as severely depleted as in P1-P3, suggesting that yet partly translocated into the PC, SMO is not activated. Similarly, in cellular models, ciliary accumulation without activation of SMO is not sufficient for Hh-signal transduction [19]. Taken together, these results suggest that the identified *SMO* variants alter the Hh pathway via instability of the protein, altered SMO trafficking to the PC or absence of SMO activation within the PC.

GLIs are the major transcriptional effectors of the Hh pathway, with GLI2 and GLI3 acting as bifunctional transcription factors that contain both an N-terminal repression domain and a C-terminal transcriptional activation domain. When the pathway is off, GLI2 and GLI3 are

targeted to the proteasome in a PC-dependent manner which promotes the processing of short forms with transcriptional repressor activity (GLI^R), $GLI3^R$ acting as the primary repressor. We thus analyzed GLI3 processing in unstimulated cells from affected individuals and found unaltered $GLI3^{FL}$ to $GLI3^R$ ratio compared to control cells (Figures 5A and 5B) in accordance with SMO-independent processing of GLI transcription factors when the pathway is off. When the pathway is on, GLI2 mediates the bulk of Hh activation whereas GLI3 processing is inhibited. We thus analyzed GLI3 processing in cells from affected individuals after activation by SAG and found no significant difference in the $GLI3^{FL}$ to $GLI3^R$ ratio between unstimulated and stimulated cells, suggesting abnormal inhibition of GLI3 processing in response to Hh pathway activation. In control cells, GLI3R appeared decreased in response to Hh stimulation, leading to increased $GLI3^{FL}$ to $GLI3^R$ ratio, yet without statistical significance (Figures 5A and 5B).

We next analyzed the ciliary trafficking of GLI2, the principal mediator of Hh-dependent transcriptional activation, and found accumulation at PC tips independently of rhSHH treatment in cells from affected individuals (Figures 5C and 5D). In fact, the number of PC with enrichment of GLI2 at the tip in either unstimulated or stimulated cells from affected individuals was approximately the same as that in control cells stimulated by rhSHH treatment (Figure 5C). This result shows constitutive GLI2 localization to the PC when SMO is defective, in agreement with animal models showing that the nuclear trafficking of GLI2 is regulated by the Hh-dependent accumulation of activated SMO within the PC. In particular, these findings are similar to those obtained in *Smo-/-* MEFs, where both GLI2 and its inhibitor partner SUFU are also enriched at PC tips independently of rhSHH stimulation [20].

The cAMP-activated kinase PKA is one of the key players in the Hh pathway, whose activity is correlated with the amount of ciliary cAMP. In the absence of Hh signal, PKA phosphorylates GLI proteins, leading to the proteolytic processing of GLI^{FL} into GLI^R. When

the pathway is on, PC accumulation of activated SMO results in the inhibition of PKA and the dissociation of GLI from their inhibitory factor SUFU allowing GLI activation and translocation into the nucleus to activate Hh target genes. Importantly, when the pathway is off, in addition to its role in GLI processing, PKA restrains the activation of GLI2 by controlling GLI-SUFU association/dissociation and trafficking within the PC [21]. We thus analyzed the subcellular localization of PKA by immunostaining. In cells from all control and affected individuals, PKA accumulates at the base of the PC (Figure S3). After treatment with forskolin (FSK), a pharmacological agent that raises intracellular cAMP levels, PKA catalytic subunit is dispersed in cells from all control and affected individuals (Figure S3), indicating normal PKA response to activating signal. In addition, we found that FSK treatment reverses rhSHH-independent GLI2 accumulation at the PC tip of cells from affected individuals, as GLI2 was not detected at the PC tip in all cells analyzed (100 cells per experiment) (Figure 5D). Whether PKA is the unique mediator of GLI2 accumulation remains to be determined, as GLI2 also disappears from the PC tip after FSK treatment in *Pka*-/- mouse cells [21].

Discussion:

Here we report biallelic loss-of-function mutations of *SMO* in individuals with a wide range of malformations. All variants we identified are either extremely rare and not observed in homozygous state ($< 10^{-5}$ alleles), or not reported in GnomAD and all missense variants are predicted to alter SMO protein function (Table 2). Of those tested, each genotype leads to severely altered Hh-signal transduction with absence of activation of Hh target genes after Hh stimulation. This depleted Hh-signal transduction is associated with reduced *SMO* expression or an altered SMO translocation to the PC in response to Hh stimulation for mutations p.(Arg261Cys), p.(Glu447*), p.(Gln764Argfs*52) and the 62 Kb deletion encompassing exon 1 of *SMO*. For variants p.(Arg576Trp) and p.(Ile429Phe) the mutant proteins are partially

translocated to the PC in response to Hh stimulation but unable to transduce the Hh signal, in accordance with their location in domains required for SMO activation (intracellular C-terminal domain) [16–18,22] or for SMO coupling to G-protein (ICL1, ICL3), both required for full activation of Hh signaling [12,13,23,24].

We also examined GLI2 and GLI3 regulation in cells from affected individuals. Concerning GLI3, the major repressor when the pathway is off, we observed unaltered $GLI3^{FL}$ to $GLI3^{R}$ ratio indicating normal proteolytic processing. This ratio remained unchanged in cells from affected individuals after Hh pathway stimulation, in accordance with previous findings *in vitro* that *Smo* knockdown or inactivation prevented Hh-mediated inhibition of Gli3 processing [25]. However, the apparent increase in $GLI3^{FL}$ to $GLI3^{R}$ ratio following stimulation in control cells remained statistically non-significant. Thus, we cannot draw conclusions on the potential involvement of GLI3 in the pathological mechanisms associated with *SMO* mutations in humans.

Concerning the ciliary trafficking of GLI2, the principal mediator of Hh-dependent transcriptional activation, GLI2 accumulates at the PC tip in cells from affected individuals independently of Hh stimulation. Thus, altered Hh signaling in cells from affected individuals is not due to altered entry of GLI2 into the PC but may be due to abnormal exit of GLI2 from the PC. This is caused by the absence of active SMO in the PC, which should lead to SUFU-GLI complex dissociation and subsequent GLI activation and translocation into the nucleus to activate Hh target genes. Furthermore, this GLI2 accumulation at the PC tip in cells from affected individuals is Hh-independent and thus may be due to an abnormal regulation of basal trafficking of GLI2, which normally shuttles in and out of the PC independently of Hh stimulation [19]. Our results suggest involvement of SMO in regulating the basal ciliary trafficking of GLI2 when the pathway is off. Interestingly, GLI2 basal trafficking has been proposed to be regulated by PKA [20]. Thus, in this model, SMO may directly or indirectly

activate PKA which in turn phosphorylates the GLI-SUFU complex to limit basal trafficking of GLI-SUFU within the PC.

All affected individuals shared postaxial polydactyly, a feature common to Hh signaling defects and to ciliopathies as the Hh pathway controls anterior to posterior growth and patterning of limb buds [26,27]. In humans, mutations in each *GLI* gene have been associated with postaxial polydactyly. In particular, in individuals with PHS, the heterozygous mutations of *GLI3* lead to a truncated protein with constitutive repressor activity leading to an excess of $GLI3^{R}$ relative to $GLI3^{A}$ and subsequent pathway under-activation [28]. Here, we found that *SMO* mutations affect mostly GLI2 trafficking resulting in Hh pathway non-activation in response to Hh stimulation.

In addition to postaxial polydactyly, three affected individuals from families F4 and F5 presented with AVSD, a cardiac malformation previously associated with ciliopathies, including Bardet-Biedl (BBS, [MIM 209900]), Meckel (MKS, [MIM 249000]) and EVC syndromes, all due to abnormal PC biogenesis and/or function [29]. The Hh pathway has long been shown crucial for cardiac septation, as exemplified by the AVSD phenotype observed in *Shh*-/- mice and conditional *Smo* mutants [30,31], as well as in other mouse models of PC gene invalidation [29,32].

Two individuals from families F3 and F4 presented with radiographic features characteristic of SRTD, in the context of JATD and EVC syndromes. Both syndromes belong to the group of skeletal ciliopathies, in which mutations in genes encoding several components of the intraflagellar transport machinery, necessary to build and maintain the PC, have been shown to be causal [33,34]. Among these genes, mutations in *IFT80* cause JATD and short rib polydactyly type III, secondary to abnormal ciliogenesis [35–37]. Interestingly, treatment with the SMO agonist SAG, as well as GLI2 overactivation, were able to rescue the osteogenic

deficiency of *IFT80*-silenced cells [37]. In addition, EVC can be caused by mutations in *EVC* and *EVC2* [38,39] encoding two proteins forming a ciliary transmembrane complex that interacts with SMO to transduce the Hh signal [40–42].

Concerning brain development, three individuals in the present report with a PHS-like phenotype have hypothalamic hamartoma and gelastic epilepsy. Both are common features in PHS, that has been strongly associated with Hh signaling defects [43]. Hypothalamic hamartoma is also one of the clinical features of oral-facial-digital (OFD) syndrome types I and VI [44,45], two syndromic ciliopathies associated with PC dysfunction with subsequent Hh signaling reduction. Conditional deletion of *Smo* in mice showed its requirement for promoting tuberal hypothalamic neuronal identity and heterogeneity among distinct hypothalamic nuclei as well as for maintenance of tuberal hypothalamic progenitors in a proliferative state [46]. However, the mechanisms underlying hypothalamic hamartoma formation in the context of reduced Hh signaling are still unknown. Corman and collaborators recently proposed a mechanism by which a non-cell autonomous gain in Hh signaling activity in wild-type cells surrounding *Smo* deleted cells (conditional deletion of *Smo* in Hh-responsive tuberal hypothalamic progenitors modeling mosaic *Smo* disruption) may cause growth of these benign tumors [46]. However, the cases we report harbor biallelic *SMO* mutations, involving all cells, and thus do not fit this model.

One individual (F2:II-1) presented with microcephaly, a feature that has also been reported in ciliopathies and is possibly associated with gyration defects. Interestingly, an appreciation of the involvement of PC and Hh signaling during neocortical development has recently emerged [47–50]. For example, Wang and collaborators nicely showed that constitutively active Shh signaling via the *SmoM2* mutation in mice led to expansion of neocortical progenitors

and induced folding of the otherwise smooth neocortex, whereas the loss of Hh signaling decreased the number of neocortical progenitors and the size of the neocortex [51].

HSCR is less commonly associated with anomalies of Hh-signal transduction or ciliopathies but is in accordance with the proposed functions of Hh signaling during gut development [52–54]. In particular, targeted deletion of *Smo* in mice as well as *Gli1* or *Shh* overexpression leads to abnormal ENS development [55–57]. HSCR has been reported in other ciliopathies or congenital anomalies of Hh-signal transduction including BBS type 1 and 4-7 [58], JATD [59], JBTS [60] and PHS [61], although the predisposition to HSCR remains low in these disorders. In individual P1, HSCR could have been explained by an additional genetic event at the *RET* locus, in which rare variations and frequent predisposing polymorphisms have been reported [62,63]. Although no *RET* coding sequence mutation was identified, P1 was heterozygous for the hypomorphic predisposing allele (rs2435357) [64]. A larger cohort of individuals with ciliopathies or developmental anomalies of Hh signaling and HSCR may allow elucidation of the genetic mechanisms leading to the HSCR trait, which may result from a mutational burden in PC genes and/or in genes encoding components of the RET signaling cascade as previously suggested in humans and zebra fish [58]. Along these lines, targeted sequencing of *GLI* genes in individuals with HSCR led to the identification of heterozygous rare variants predicted to be damaging yet inherited from unaffected parents [65]. While these may not be sufficient alone to cause the phenotype, they may contribute to a higher mutational load in the RET/Hh signaling pathways and/or PC genes [65,66].

Finally, ocular anomalies were not reported in this study whereas recently, compound heterozygous missense *SMO* mutations were recently reported in a child with both anterior segment dysgenesis (congenital corneal opacity, cataract) and morning glory syndrome, without other ciliopathy-like phenotypes [67]. In mice, conditional *Smo* deletion results in lens

and corneal defects from E14.5 [68], thus supporting dysfunction of *SMO* as responsible for the ocular anomalies observed, although functional data concerning the pathogenicity of the variants reported by Zhang *et al* is required.

Altogether, we here report biallelic loss-of-function *SMO* mutations in human resulting in a broad spectrum of developmental anomalies affecting the brain (hypothalamic hamartoma, microcephaly), the heart (AVSD), the skeleton (postaxial polydactyly, narrow chest, shortening of long bones) and the gut (aganglionosis). Functional analysis in cells from affected individuals indicated severely impaired transduction of the Hh signaling pathway and altered PC trafficking of GLI2. Our results expand the range of human pathologies caused by alteration of SMO, which in addition to somatic mutations that cause cancer, now includes germline mutations leading to a developmental disorder.

Declaration of interests

The authors declare no competing interests.

Acknowledgements

We are grateful to the affected individuals and their families for their participation. We thank Marc Le Loch for helping with targeted resequencing and Megan Cho for scientific networking. This work was supported by grants from the 'Agence Nationale de la Recherche' (ANR) to ST (ANR-17-CE16-0003-01), from MSDAvenir (DevoDecode project), and the 'Fondation Maladies Rares' (HTS-RD-I20140502). TLL is supported by the French Excellence Program of the French Ambassy in Vietnam and the Fondation pour la Recherche Médicale (Ph.D. program). The *Imagine* Institute is supported by State funding from the ANR under "Investissements d'avenir" program (ANR-10-IAHU-01) and as part of the second "Investissements d'Avenir" program (ANR-17-RHUS-0002). The research conducted at the Murdoch Children's Research Institute was supported by the Victorian Government's Operational Infrastructure Support Program.

Supplemental Data description

Supplemental Data include 3 figures and 3 tables.

Web Resources

GnomAD: https://gnomad.broadinstitute.org/faq;

Decipher: https://decipher.sanger.ac.uk

UCSC Genome Browser: http://genome.ucsc.edu;

Primer3plus: https://primer3plus.com

Polyphen-2: http://genetics.bwh.harvard.edu/pph/

Sift: https://sift.bii.a-star.edu.sg

CADD: https://cadd.gs.washington.edu

Chimera : https://www.cgl.ucsf.edu/chimera/

RCSB PDB : http://www.rcsb.org/

OMIM : https://www.ncbi.nlm.nih.gov/omim

References

1. Huangfu, D., Liu, A., Rakeman, A.S., Murcia, N.S., Niswander, L., and Anderson, K.V. (2003). Hedgehog signalling in the mouse requires intraflagellar transport proteins. Nature *426*, 83–87.
2. Goetz, S.C., and Anderson, K.V. (2010). The primary cilium: a signalling centre during vertebrate development. Nat. Rev. Genet. *11*, 331–344.
3. Corbit, K.C., Shyer, A.E., Dowdle, W.E., Gaulden, J., Singla, V., Chen, M.-H., Chuang, P.-T., and Reiter, J.F. (2008). Kif3a constrains beta-catenin-dependent Wnt signalling through dual ciliary and non-ciliary mechanisms. Nat. Cell Biol. *10*, 70–76.
4. Rohatgi, R., Milenkovic, L., and Scott, M.P. (2007). Patched1 regulates hedgehog signaling at the primary cilium. Science *317*, 372–376.
5. Santos, N., and Reiter, J.F. (2014). A central region of Gli2 regulates its localization to the primary cilium and transcriptional activity. J. Cell. Sci. *127*, 1500–1510.
6. Palencia-Campos, A., Ullah, A., Nevado, J., Yildirim, R., Unal, E., Ciorraga, M., Barruz, P., Chico, L., Piceci-Sparascio, F., Guida, V., et al. (2017). GLI1 inactivation is associated with developmental phenotypes overlapping with Ellis-van Creveld syndrome. Hum. Mol. Genet. *26*, 4556–4571.
7. França, M.M., Jorge, A.A.L., Carvalho, L.R.S., Costalonga, E.F., Vasques, G.A., Leite, C.C., Mendonca, B.B., and Arnhold, I.J.P. (2010). Novel heterozygous nonsense GLI2 mutations in patients with hypopituitarism and ectopic posterior pituitary lobe without holoprosencephaly. J. Clin. Endocrinol. Metab. *95*, E384-391.
8. Xie, J., Murone, M., Luoh, S.M., Ryan, A., Gu, Q., Zhang, C., Bonifas, J.M., Lam, C.W., Hynes, M., Goddard, A., et al. (1998). Activating Smoothened mutations in sporadic basal-cell carcinoma. Nature *391*, 90–92.
9. Twigg, S.R.F., Hufnagel, R.B., Miller, K.A., Zhou, Y., McGowan, S.J., Taylor, J., Craft, J., Taylor, J.C., Santoro, S.L., Huang, T., et al. (2016). A Recurrent Mosaic Mutation in SMO, Encoding the Hedgehog Signal Transducer Smoothened, Is the Major Cause of Curry-Jones Syndrome. Am. J. Hum. Genet. *98*, 1256–1265.
10. Sobreira, N., Schiettecatte, F., Valle, D., and Hamosh, A. (2015). GeneMatcher: a matching tool for connecting investigators with an interest in the same gene. Hum. Mutat. *36*, 928–930.
11. Rosain, J., Oleaga-Quintas, C., Deswarte, C., Verdin, H., Marot, S., Syridou, G., Mansouri, M., Mahdaviani, S.A., Venegas-Montoya, E., Tsolia, M., et al. (2018). A Variety of Alu-Mediated Copy Number Variations Can Underlie IL-12Rβ1 Deficiency. J. Clin. Immunol. *38*, 617–627.
12. Qi, X., Liu, H., Thompson, B., McDonald, J., Zhang, C., and Li, X. (2019). Cryo-EM structure of oxysterol-bound human Smoothened coupled to a heterotrimeric Gi. Nature *571*, 279–283.
13. Ogden, S.K., Fei, D.L., Schilling, N.S., Ahmed, Y.F., Hwa, J., and Robbins, D.J. (2008). G protein Galphai functions immediately downstream of Smoothened in Hedgehog signalling. Nature *456*, 967–970.
14. Byrne, E.F.X., Sircar, R., Miller, P.S., Hedger, G., Luchetti, G., Nachtergaele, S., Tully, M.D., Mydock-McGrane, L., Covey, D.F., Rambo, R.P., et al. (2016). Structural basis of Smoothened regulation by its extracellular domains. Nature *535*, 517–522.
15. Rubino, S., Qian, J., Pinheiro-Neto, C.D., Kenning, T.J., and Adamo, M.A. (2018). A familial syndrome of hypothalamic hamartomas, polydactyly, and SMO mutations: a clinical report of 2 cases. J Neurosurg Pediatr *23*, 98–103.
16. Chen, Y., Sasai, N., Ma, G., Yue, T., Jia, J., Briscoe, J., and Jiang, J. (2011). Sonic Hedgehog dependent phosphorylation by CK1α and GRK2 is required for ciliary

accumulation and activation of smoothened. PLoS Biol. *9*, e1001083.
17. Zhang, C., Williams, E.H., Guo, Y., Lum, L., and Beachy, P.A. (2004). Extensive phosphorylation of Smoothened in Hedgehog pathway activation. Proc. Natl. Acad. Sci. U.S.A. *101*, 17900–17907.
18. Varjosalo, M., Li, S.-P., and Taipale, J. (2006). Divergence of hedgehog signal transduction mechanism between Drosophila and mammals. Dev. Cell *10*, 177–186.
19. Kim, J., Kato, M., and Beachy, P.A. (2009). Gli2 trafficking links Hedgehog-dependent activation of Smoothened in the primary cilium to transcriptional activation in the nucleus. Proc. Natl. Acad. Sci. U.S.A. *106*, 21666–21671.
20. Tukachinsky, H., Lopez, L.V., and Salic, A. (2010). A mechanism for vertebrate Hedgehog signaling: recruitment to cilia and dissociation of SuFu-Gli protein complexes. J. Cell Biol. *191*, 415–428.
21. Tuson, M., He, M., and Anderson, K.V. (2011). Protein kinase A acts at the basal body of the primary cilium to prevent Gli2 activation and ventralization of the mouse neural tube. Development *138*, 4921–4930.
22. Jiang, K., Liu, Y., Fan, J., Zhang, J., Li, X.-A., Evers, B.M., Zhu, H., and Jia, J. (2016). PI(4)P Promotes Phosphorylation and Conformational Change of Smoothened through Interaction with Its C-terminal Tail. PLoS Biol. *14*, e1002375.
23. Nakano, Y., Nystedt, S., Shivdasani, A.A., Strutt, H., Thomas, C., and Ingham, P.W. (2004). Functional domains and sub-cellular distribution of the Hedgehog transducing protein Smoothened in Drosophila. Mech. Dev. *121*, 507–518.
24. Buck, F., Wang, W., Harder, S., Brathwaite, C., Bruhn, T.O., and Gershengorn, M.C. (2000). Juxtamembrane regions in the third intracellular loop of the thyrotropin-releasing hormone receptor type 1 are important for coupling to Gq. Endocrinology *141*, 3717–3722.
25. Wen, X., Lai, C.K., Evangelista, M., Hongo, J.-A., de Sauvage, F.J., and Scales, S.J. (2010). Kinetics of hedgehog-dependent full-length Gli3 accumulation in primary cilia and subsequent degradation. Mol. Cell. Biol. *30*, 1910–1922.
26. Verma, P.K., and El-Harouni, A.A. (2015). Review of literature: genes related to postaxial polydactyly. Front Pediatr *3*, 8.
27. Tickle, C., and Towers, M. (2017). Sonic Hedgehog Signaling in Limb Development. Front Cell Dev Biol *5*, 14.
28. Shin, S.H., Kogerman, P., Lindström, E., Toftgård, R., and Biesecker, L.G. (1999). GLI3 mutations in human disorders mimic Drosophila cubitus interruptus protein functions and localization. Proc. Natl. Acad. Sci. U.S.A. *96*, 2880–2884.
29. Burnicka-Turek, O., Steimle, J.D., Huang, W., Felker, L., Kamp, A., Kweon, J., Peterson, M., Reeves, R.H., Maslen, C.L., Gruber, P.J., et al. (2016). Cilia gene mutations cause atrioventricular septal defects by multiple mechanisms. Hum. Mol. Genet. *25*, 3011–3028.
30. Goddeeris, M.M., Rho, S., Petiet, A., Davenport, C.L., Johnson, G.A., Meyers, E.N., and Klingensmith, J. (2008). Intracardiac septation requires hedgehog-dependent cellular contributions from outside the heart. Development *135*, 1887–1895.
31. Lin, L., Bu, L., Cai, C.-L., Zhang, X., and Evans, S. (2006). Isl1 is upstream of sonic hedgehog in a pathway required for cardiac morphogenesis. Dev. Biol. *295*, 756–763.
32. Willaredt, M.A., Gorgas, K., Gardner, H.A.R., and Tucker, K.L. (2012). Multiple essential roles for primary cilia in heart development. Cilia *1*, 23.
33. Huber, C., and Cormier-Daire, V. (2012). Ciliary disorder of the skeleton. Am J Med Genet C Semin Med Genet *160C*, 165–174.
34. Schmidts, M., Hou, Y., Cortés, C.R., Mans, D.A., Huber, C., Boldt, K., Patel, M., van Reeuwijk, J., Plaza, J.-M., van Beersum, S.E.C., et al. (2015). TCTEX1D2 mutations underlie Jeune asphyxiating thoracic dystrophy with impaired retrograde intraflagellar transport. Nat Commun *6*, 7074.

35. Beales, P.L., Bland, E., Tobin, J.L., Bacchelli, C., Tuysuz, B., Hill, J., Rix, S., Pearson, C.G., Kai, M., Hartley, J., et al. (2007). IFT80, which encodes a conserved intraflagellar transport protein, is mutated in Jeune asphyxiating thoracic dystrophy. Nat. Genet. *39*, 727–729.
36. Cavalcanti, D.P., Huber, C., Sang, K.-H.L.Q., Baujat, G., Collins, F., Delezoide, A.-L., Dagoneau, N., Le Merrer, M., Martinovic, J., Mello, M.F.S., et al. (2011). Mutation in IFT80 in a fetus with the phenotype of Verma-Naumoff provides molecular evidence for Jeune-Verma-Naumoff dysplasia spectrum. J. Med. Genet. *48*, 88–92.
37. Yang, S., and Wang, C. (2012). The intraflagellar transport protein IFT80 is required for cilia formation and osteogenesis. Bone *51*, 407–417.
38. Galdzicka, M., Patnala, S., Hirshman, M.G., Cai, J.-F., Nitowsky, H., Egeland, J.A., and Ginns, E.I. (2002). A new gene, EVC2, is mutated in Ellis-van Creveld syndrome. Mol. Genet. Metab. *77*, 291–295.
39. Ruiz-Perez, V.L., Tompson, S.W.J., Blair, H.J., Espinoza-Valdez, C., Lapunzina, P., Silva, E.O., Hamel, B., Gibbs, J.L., Young, I.D., Wright, M.J., et al. (2003). Mutations in two nonhomologous genes in a head-to-head configuration cause Ellis-van Creveld syndrome. Am. J. Hum. Genet. *72*, 728–732.
40. Caparrós-Martín, J.A., Valencia, M., Reytor, E., Pacheco, M., Fernandez, M., Perez-Aytes, A., Gean, E., Lapunzina, P., Peters, H., Goodship, J.A., et al. (2013). The ciliary Evc/Evc2 complex interacts with Smo and controls Hedgehog pathway activity in chondrocytes by regulating Sufu/Gli3 dissociation and Gli3 trafficking in primary cilia. Hum. Mol. Genet. *22*, 124–139.
41. Dorn, K.V., Hughes, C.E., and Rohatgi, R. (2012). A Smoothened-Evc2 complex transduces the Hedgehog signal at primary cilia. Dev. Cell *23*, 823–835.
42. Yang, C., Chen, W., Chen, Y., and Jiang, J. (2012). Smoothened transduces Hedgehog signal by forming a complex with Evc/Evc2. Cell Res. *22*, 1593–1604.
43. Hildebrand, M.S., Griffin, N.G., Damiano, J.A., Cops, E.J., Burgess, R., Ozturk, E., Jones, N.C., Leventer, R.J., Freeman, J.L., Harvey, A.S., et al. (2016). Mutations of the Sonic Hedgehog Pathway Underlie Hypothalamic Hamartoma with Gelastic Epilepsy. Am. J. Hum. Genet. *99*, 423–429.
44. Poretti, A., Vitiello, G., Hennekam, R.C.M., Arrigoni, F., Bertini, E., Borgatti, R., Brancati, F., D'Arrigo, S., Faravelli, F., Giordano, L., et al. (2012). Delineation and diagnostic criteria of Oral-Facial-Digital Syndrome type VI. Orphanet J Rare Dis *7*, 4.
45. Azukizawa, T., Yamamoto, M., Narumiya, S., and Takano, T. (2013). Oral-facial-digital syndrome type 1 with hypothalamic hamartoma and Dandy-Walker malformation. Pediatr. Neurol. *48*, 329–332.
46. Corman, T.S., Bergendahl, S.E., and Epstein, D.J. (2018). Distinct temporal requirements for Sonic hedgehog signaling in development of the tuberal hypothalamus. Development *145*,.
47. Thomas, S., Boutaud, L., Reilly, M.L., and Benmerah, A. (2019). Cilia in hereditary cerebral anomalies. Biol. Cell *111*, 217–231.
48. Park, S.M., Jang, H.J., and Lee, J.H. (2019). Roles of Primary Cilia in the Developing Brain. Front Cell Neurosci *13*, 218.
49. Guo, J., Higginbotham, H., Li, J., Nichols, J., Hirt, J., Ghukasyan, V., and Anton, E.S. (2015). Developmental disruptions underlying brain abnormalities in ciliopathies. Nat Commun *6*, 7857.
50. Taverna, E., Götz, M., and Huttner, W.B. (2014). The cell biology of neurogenesis: toward an understanding of the development and evolution of the neocortex. Annu. Rev. Cell Dev. Biol. *30*, 465–502.
51. Wang, L., Hou, S., and Han, Y.-G. (2016). Hedgehog signaling promotes basal progenitor expansion and the growth and folding of the neocortex. Nat. Neurosci. *19*, 888–896.

52. Sukegawa, A., Narita, T., Kameda, T., Saitoh, K., Nohno, T., Iba, H., Yasugi, S., and Fukuda, K. (2000). The concentric structure of the developing gut is regulated by Sonic hedgehog derived from endodermal epithelium. Development *127*, 1971–1980.
53. Fu, M., Lui, V.C.H., Sham, M.H., Pachnis, V., and Tam, P.K.H. (2004). Sonic hedgehog regulates the proliferation, differentiation, and migration of enteric neural crest cells in gut. J. Cell Biol. *166*, 673–684.
54. Nagy, N., Barad, C., Graham, H.K., Hotta, R., Cheng, L.S., Fejszak, N., and Goldstein, A.M. (2016). Sonic hedgehog controls enteric nervous system development by patterning the extracellular matrix. Development *143*, 264–275.
55. Huang, H., Cotton, J.L., Wang, Y., Rajurkar, M., Zhu, L.J., Lewis, B.C., and Mao, J. (2013). Specific requirement of Gli transcription factors in Hedgehog-mediated intestinal development. J. Biol. Chem. *288*, 17589–17596.
56. Ramalho-Santos, M., Melton, D.A., and McMahon, A.P. (2000). Hedgehog signals regulate multiple aspects of gastrointestinal development. Development *127*, 2763–2772.
57. Yang, J.T., Liu, C.Z., Villavicencio, E.H., Yoon, J.W., Walterhouse, D., and Iannaccone, P.M. (1997). Expression of human GLI in mice results in failure to thrive, early death, and patchy Hirschsprung-like gastrointestinal dilatation. Mol. Med. *3*, 826–835.
58. de Pontual, L., Zaghloul, N.A., Thomas, S., Davis, E.E., McGaughey, D.M., Dollfus, H., Baumann, C., Bessling, S.L., Babarit, C., Pelet, A., et al. (2009). Epistasis between RET and BBS mutations modulates enteric innervation and causes syndromic Hirschsprung disease. Proc. Natl. Acad. Sci. U.S.A. *106*, 13921–13926.
59. Aurora, P., and Wallis, C.E. (1999). Jeune syndrome (asphyxiating thoracic dystrophy) associated with Hirschsprung disease. Clin. Dysmorphol. *8*, 259–263.
60. Ozyurek, H., Kayacik, O.E., Gungor, O., and Karagoz, F. (2008). Rare association of Hirschsprung's disease and Joubert syndrome. Eur. J. Pediatr. *167*, 475–477.
61. Li, M.H., Eberhard, M., Mudd, P., Javia, L., Zimmerman, R., Khalek, N., and Zackai, E.H. (2015). Total colonic aganglionosis and imperforate anus in a severely affected infant with Pallister-Hall syndrome. Am. J. Med. Genet. A *167A*, 617–620.
62. Edery, P., Lyonnet, S., Mulligan, L.M., Pelet, A., Dow, E., Abel, L., Holder, S., Nihoul-Fékété, C., Ponder, B.A., and Munnich, A. (1994). Mutations of the RET proto-oncogene in Hirschsprung's disease. Nature *367*, 378–380.
63. Amiel, J., Sproat-Emison, E., Garcia-Barcelo, M., Lantieri, F., Burzynski, G., Borrego, S., Pelet, A., Arnold, S., Miao, X., Griseri, P., et al. (2008). Hirschsprung disease, associated syndromes and genetics: a review. J. Med. Genet. *45*, 1–14.
64. Emison, E.S., Garcia-Barcelo, M., Grice, E.A., Lantieri, F., Amiel, J., Burzynski, G., Fernandez, R.M., Hao, L., Kashuk, C., West, K., et al. (2010). Differential contributions of rare and common, coding and noncoding Ret mutations to multifactorial Hirschsprung disease liability. Am. J. Hum. Genet. *87*, 60–74.
65. Liu, J.A.-J., Lai, F.P.-L., Gui, H.-S., Sham, M.-H., Tam, P.K.-H., Garcia-Barcelo, M.-M., Hui, C.-C., and Ngan, E.S.-W. (2015). Identification of GLI Mutations in Patients With Hirschsprung Disease That Disrupt Enteric Nervous System Development in Mice. Gastroenterology *149*, 1837-1848.e5.
66. Young, H.M., Stamp, L.A., and Hofstra, R.M.W. (2015). Hirschsprung Disease and Activation of Hedgehog Signaling via GLI1-3 Mutations. Gastroenterology *149*, 1672–1675.
67. Zhang, J., Li, Y., Fan, Y., Wu, D., and Xu, J. (2019). Compound heterozygous mutations in SMO associated with anterior segment dysgenesis and morning glory syndrome. Gene *713*, 143973.
68. Choi, J.J.Y., Ting, C.-T., Trogrlic, L., Milevski, S.V., Familari, M., Martinez, G., and de Iongh, R.U. (2014). A role for smoothened during murine lens and cornea development. PLoS ONE *9*, e108037.

Figure titles and legends

Figure 1. Clinical features of affected individuals. Brain MRI sections on axial T1 (A1, B1, C1) and sagittal T1 (A2, B2, C2) show hypothalamic hamartoma in P1-P3 (yellow stars). P1 had postaxial polydactyly of lower limbs (A3, A4). P2 and P3 had bilateral postaxial polydactyly of lower limbs with scars on the 5th digits after surgical removal of the 6th digits (B3, B4). P3 also had syndactyly of the 2nd and 3rd digits of both feet (C3, C4). P4 had short-limbed disproportionate short stature, with narrow thoracic cage (D1), postaxial polydactyly with hypoplasia of middle and distal phalanges and Y-shaped metatarsal (D2, D3), paired sublingual fleshy appendages surgically resected in infancy (D4), trident pelvis with thick pubic and ischial bones (D5), short ribs with metaphyseal cupping (D6), ovoid vertebral bodies (D7), short long bones with metaphyseal lucency and sclerosis (D8). P5 presented with complete AVSD (not shown), long and narrow thorax (E1), oligodontia (E2), trident acetabular roof (E3), postaxial polydactyly of both hands (E4,E5) and Y-shaped metatarsal of the left foot (E6). P6 and P7 had AVSD (not shown), postaxial polydactyly of all four limbs (F1-G4) and 2/3 syndactyly of both feet (G3,G4).

Figure 2. Pedigrees of the five families carrying *SMO* biallelic variations. *SMO* variants are reported based on Human Genome Assembly GRCh37 (hg19), the *SMO* reference sequence used was NM_005631.4. *SMO* variants were confirmed by Sanger sequencing on genomic DNA extracted from peripheral blood samples or fibroblasts of affected individuals and their parents. All variants segregated as expected from an autosomal recessive mode of inheritance in all available family members. In P2 from family F2, a large heterozygous deletion encompassing *SMO* and *TSPAN33* inherited from the mother was identified by targeted sequencing of a region of 153 Kb (7q32.1: 128773868-128927701). DNA breakpoints mapped to AluSx and AluSz repeats (red boxes) located at the borders of the deleted region (chr7 g.128778292_128840690del).

Figure 3. Effects of *SMO* variants on the expression of *SMO* at the mRNA level. (A) Quantification of *SMO* mRNA level by quantitative Real Time PCR (qrtPCR) showed an expression decreased by 50 to 60% in P1-P4 compared to controls and an expression similar to controls in P6 and P7. qrtPCR was performed using primers specific to *SMO* transcript on mRNA extracted from fibroblasts of affected individuals and two unrelated age-matched controls. Data from three independent experiments were normalized to *GUSB* and *HPRT* mRNA levels, analyzed with the $2^{-\Delta\Delta Ct}$ method and presented as mean values ±SEM. **p<0.05; ***p<0.001 (Kruskal-Wallis test). (B) Sanger sequencing on cDNA from P1-P4, P6 and P7. Missense variants are indicated in black boxes and deletion or splicing variant by black lines. For P4, both canonical and cryptic splice sites are indicated and red box highlights the skipped region. (C-F) 3D modeling of the identified variants on the active G_i-coupled human SMO crystal structure (PDB ID: 6OT0). The Arg261 and Ile429 residues are located at the ICL1 and ICL3, respectively (C, D). The predicted truncated protein terminating at the Glu447 residue lacks all the TM6, TM7, ECL3 and the C-terminal intracellular tail of SMO (C). The Arg576 in the C-terminal tail of SMO corresponding to Arg580 in mSmo, is a critical residue required for downstream signaling (C). The c.2291_2292delAG causes a frameshift leading to a truncated SMO lacking the distal C-terminal tail of SMO, highly conserved throughout evolution and comprising two phosphorylation sites (Ser771 and Ser785, red arrowheads) involved in SMO activation, mapped to aligned sequences of human (h), mouse (m), zebrafish (z) and xenopus (x) SMO proteins (C). Structural comparison of G_i-coupled hSMO and inactive hSMO (PDB ID: 5L7D) showed different conformations of the Arg261 (blue for active and purple for inactive conformations) (E). The substitution of Arg to Cys at amino acid 261 modified the distance of the hydrogen bond (in red) between this residue and the Tyr262 (F).

Figure 4. Normal ciliogenesis but altered Hh signaling transduction and SMO trafficking in cells from affected individuals. (A, B) Representative images and quantification of ciliogenesis in cells form controls and affected individuals. PC protruded from most cells of controls and affected individuals (~100 cells analyzed in three independent experiments). The percentage of ciliated cells was calculated by dividing PC counts by nuclei counts. Data are summarized in bar charts (mean values ± SEM) in (B). (C) Measurement of PC length after 3D reconstruction showed normal PC length in cells from affected individuals as compared to controls. Data represented in box and whisker plots are from three independent experiments (~100 cells analyzed per experiment). (D) Assessment of the Hh-signal transduction by quantification of the induction of two Hh target genes *GLI1* and *PTCH1* on Hh-stimulated cells from controls and effected individuals. The expression of both genes is normally induced in controls whereas no induction is found in any of affected individuals tested. Values were presented as relative expression levels ± SEM. Dashed red line indicates no induction of *GLI1* or *PTCH1* expression (ratio of stimulated versus unstimulated normalized expression = 1). $^{**}p < 0.0001$ (Kolmogorov-Smirnov test). (E) Representative images and (F) quantification of endogenous PC translocation of SMO in Hh-stimulated cells from control and affected individuals by adding rhSHH (+rhSHH) or without stimulation (-rhSHH). IF analysis showed altered translocation of SMO to the PC in P1, P2 and P3 after Hh pathway induction as compared to controls. In P4 and P6, SMO appears translocated to the PC while the percentage of positive SMO PC appears significantly diminished as compared to controls. Data from three independent experiments are summarized in bar charts (mean values ± SEM). ****p<0.0001 (Fisher exact test). Scale bars = 5µm.

Figure 5. GLI2 and GLI3 regulation in cells of individuals harboring *SMO* variants.

Image (A) and quantification (B) of Western blot analysis on proteins extracted from cells of affected individuals and controls showed that the $GLI3^{FL}$:$GLI3^{R}$ ratio remained unchanged between unstimulated and stimulated cells from affected individuals. The $GLI3^{FL}$:$GLI3^{R}$ ratio in control cells increased after SAG-stimulation compared to unstimulated cells without statistical significance. GAPDH was used as a loading control. Data is presented as mean value ±SEM and statistical analysis was performed using Kruskal-Wallis test. (C-D) Representative images and quantification of GLI2 positive PC in cells from controls and affected individuals. In unstimulated control cells (-rhSHH), GLI2 is detectable at 30% of PC tips, whereas upon Hh stimulation (+rhSHH), GLI2 accumulates at the PC tips in 75% of cells. In cells of all affected individuals, GLI2 accumulates at the PC tips independently of Hh-stimulation (85-90% of PC). Data from three independent experiments (~100 cells analyzed per experiment) are presented as mean value ±SEM. ***$p<0.001$, ****$p<0.0001$ (Fisher Exact Test). Scale bar = 3µm.

Affected Individuals	**F1-II:1 (P1)**	**F2-II:1 (P2)**	**F2-II:2 (P3)**	**F3-II:1 (P4)**	**F4 – II:4 (P5)**	**F5-II:2 (P6)**	**F5-II:3 (P7)**
Gender	Male	Male	Male	Male	Male	Male	Female
Age at last examination	3y	7y	4y	5y	8y	Deceased at 3 months	8y
Psychomotor Development	Normal	Normal	Normal	Mild delay	Normal	NR	Normal
Gelastic epilepsy	+	+	+	-	-	-	-
Hypothalamic hamartoma	+	+	+	-	-	NA	NA
Microcephaly	-	+	-	-	-	-	-
Dysmorphic facial features	+	+	+	+	-	-	-
Chest/Rib abnormalities	-	-	-	+	moderate	-	-
Postaxial polydactyly	+	+	+	+	+	+	+
Syndactyly	-	5/6	2/3	5/6	-	2/3	2/3
Cardiac defect	-	-	-	-	+	+	+
Hirschsprung disease	+	-	-	-	-	-	-

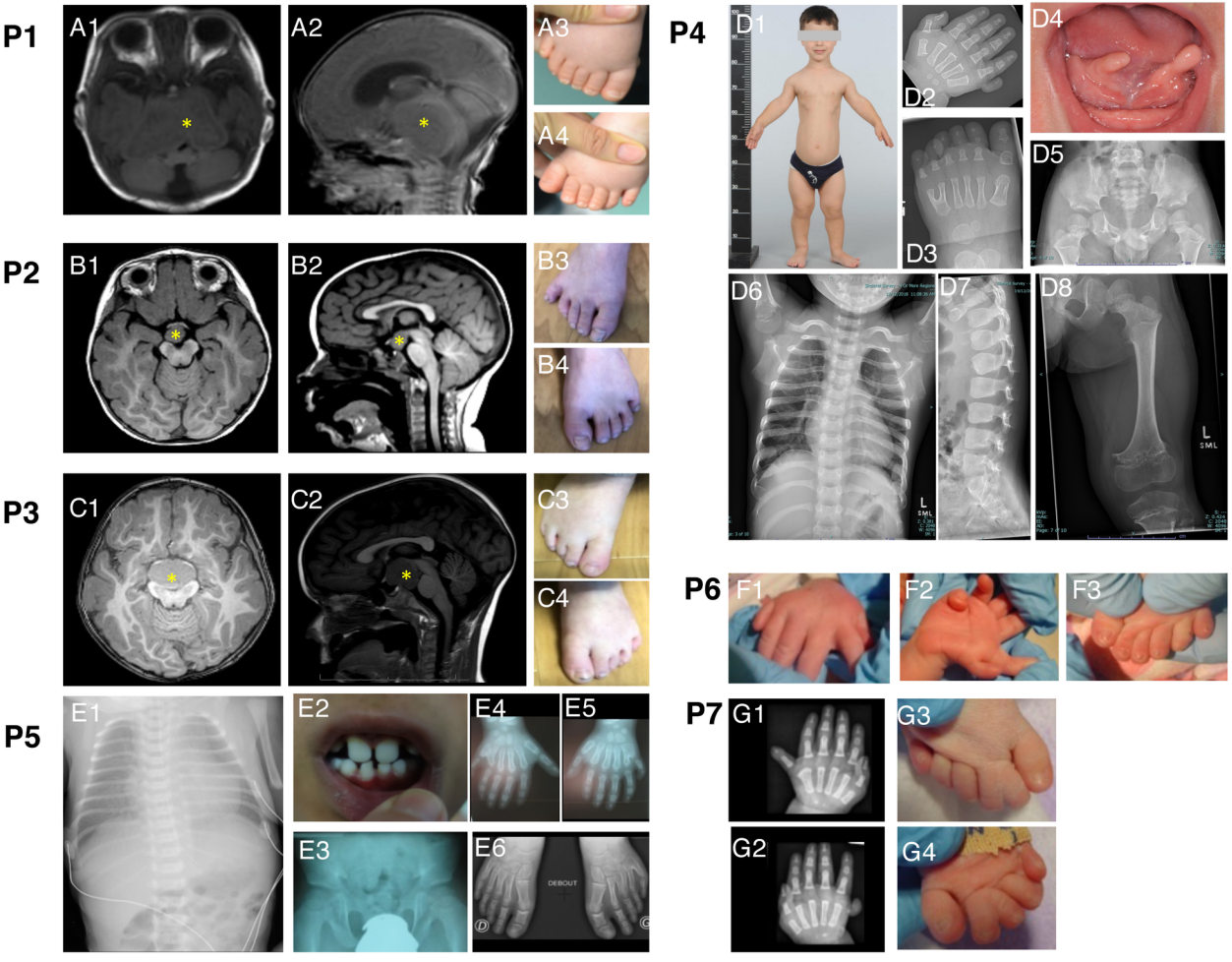
Abbreviations: NA = not available, NR = not relevant

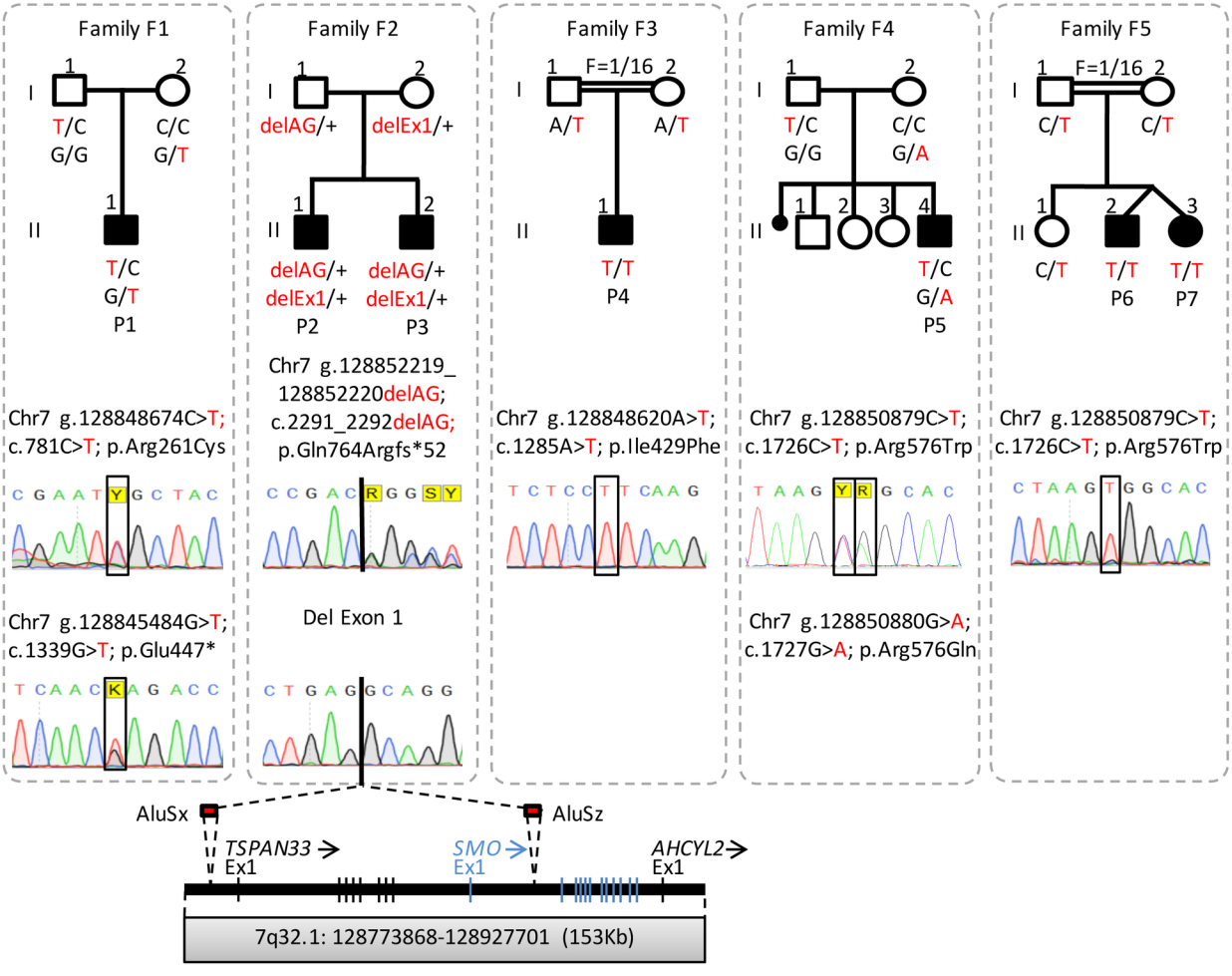
Table 1: Clinical description of Individuals with biallelic variants in *SMO*

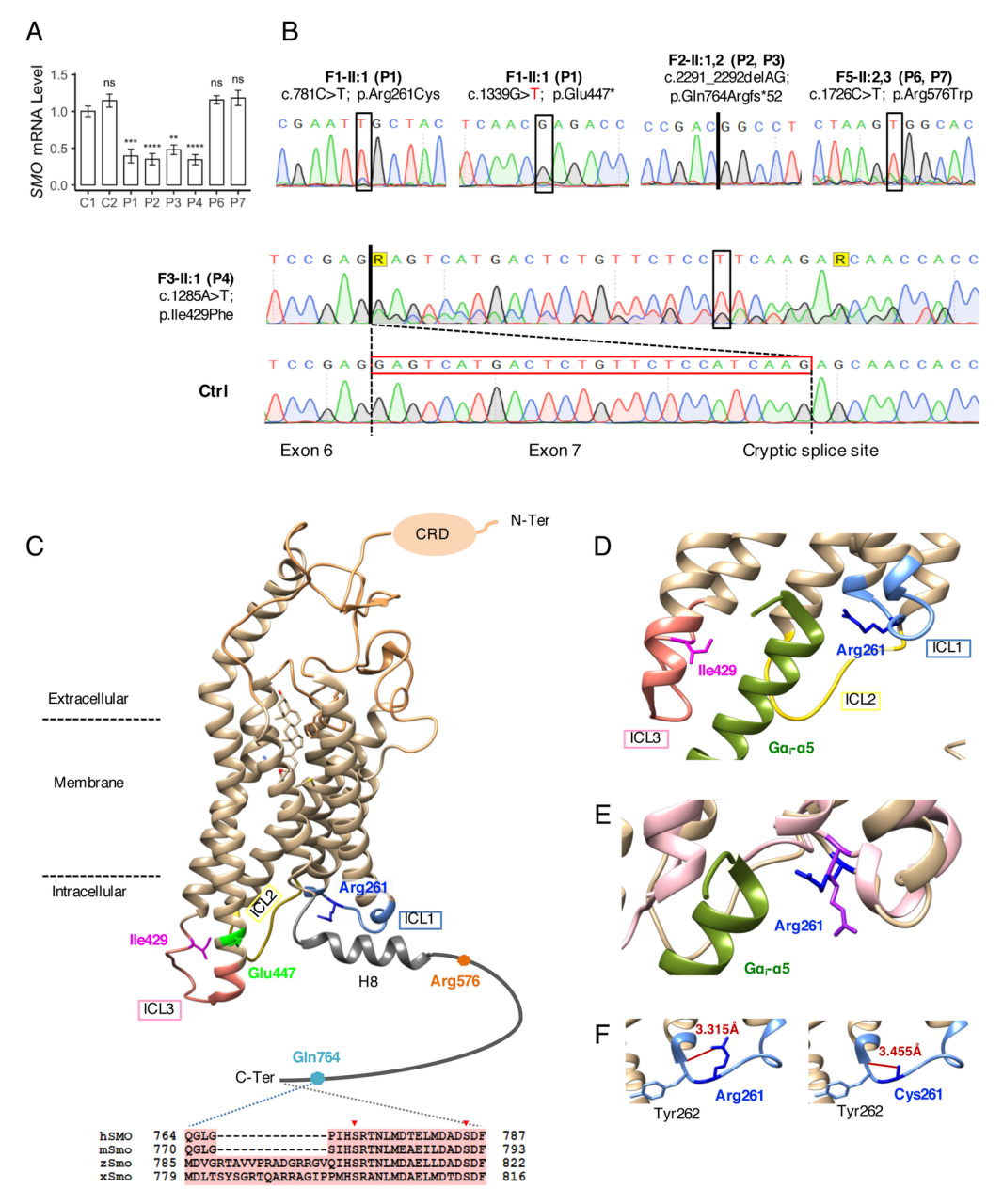
Individuals	Genomic Position (hg19)	cDNA (NM_005631.4)	Protein	gnomAD v2.1.1	CADD v4.1	SIFT	Polyphen2	Inheritance
F1-II:1	Chr7:128845484C>T	c.781C>T	p.Arg261Cys	1/121411/0	34	Deleterious (0.01)	Disease causing (1)	Comp. Htz.
	Chr7:128848674G>T	c.1339G>T	p.Glu447*	0	44			Comp. Htz.
F2-II:1 and 2	Chr7:128778292_ 128840690del							Comp. Htz.
	Chr7:128852219_ 128852220del	c.2291_ 2292del	p.Gln764Argfs*52	0				Comp. Htz.
F3-II:1	Chr7 :128848620A>T	c.1285A>T	p.Ile429Phe	0	27.3	Deleterious (0.03)	Disease causing (1)	Hmz.
F4-II:4	Chr7:128850880G>A	c.1727G>A	p.Arg576Gln	1/251186/0	33	Deleterious (0)	Disease causing (1)	Comp. Htz.
	Chr7:128850879C>T	c.1726C>T	p.Arg576Trp	2/121410/0	33	Deleterious (0)	Disease causing (1)	Comp. Htz.
F5-II:2 and 3	Chr7:128850879C>T	c.1726C>T	p.Arg576Trp	2/121410/0	33	Deleterious (0)	Disease causing (1)	Hmz.

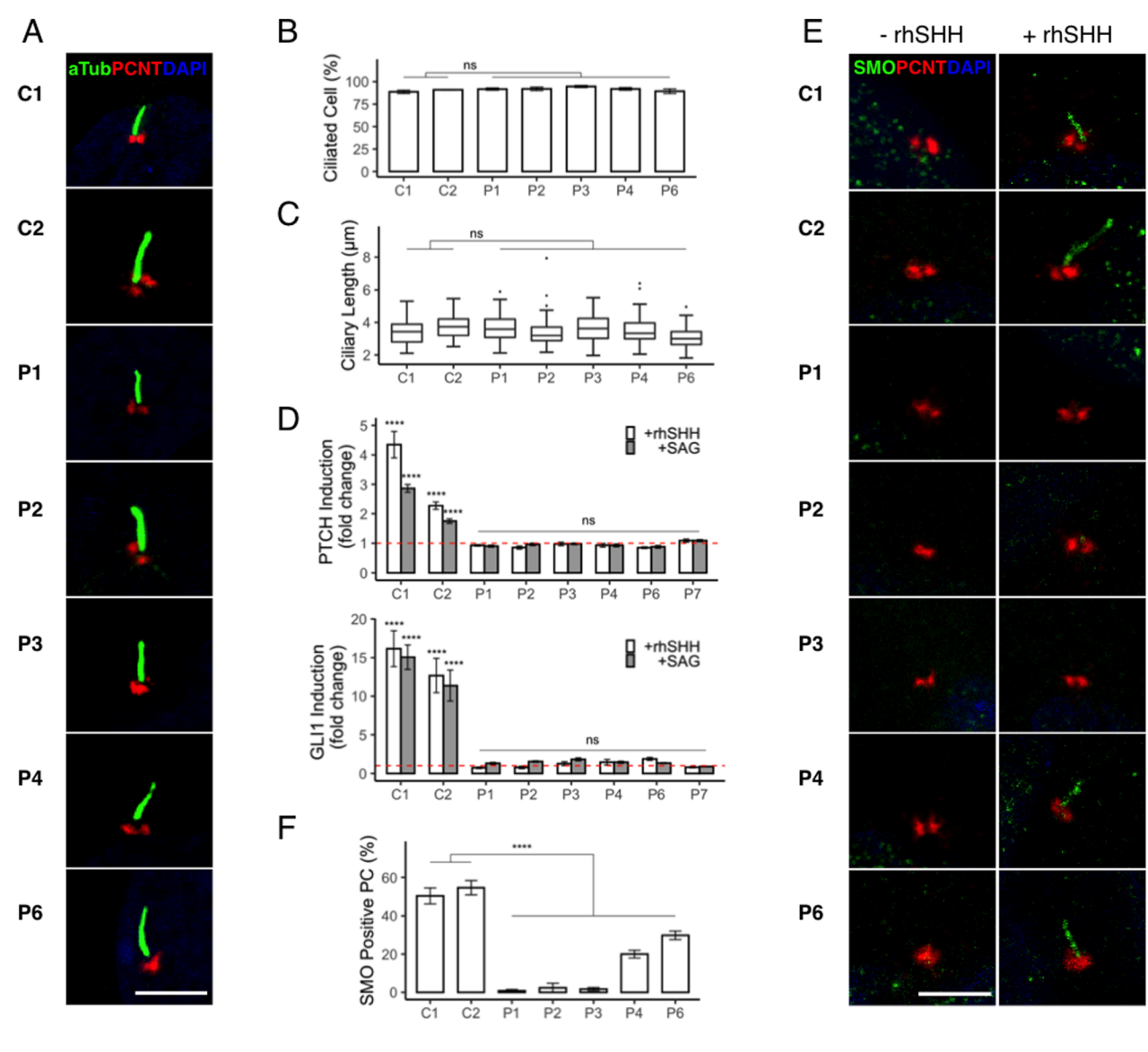
Abbreviations: Comp. Htz. = compound heterozygous; Hmz. = homozygous; CADD = Combined Annotation Dependent Depletion. gnomAD data are presented as allele count/allele number/number of Hmz.

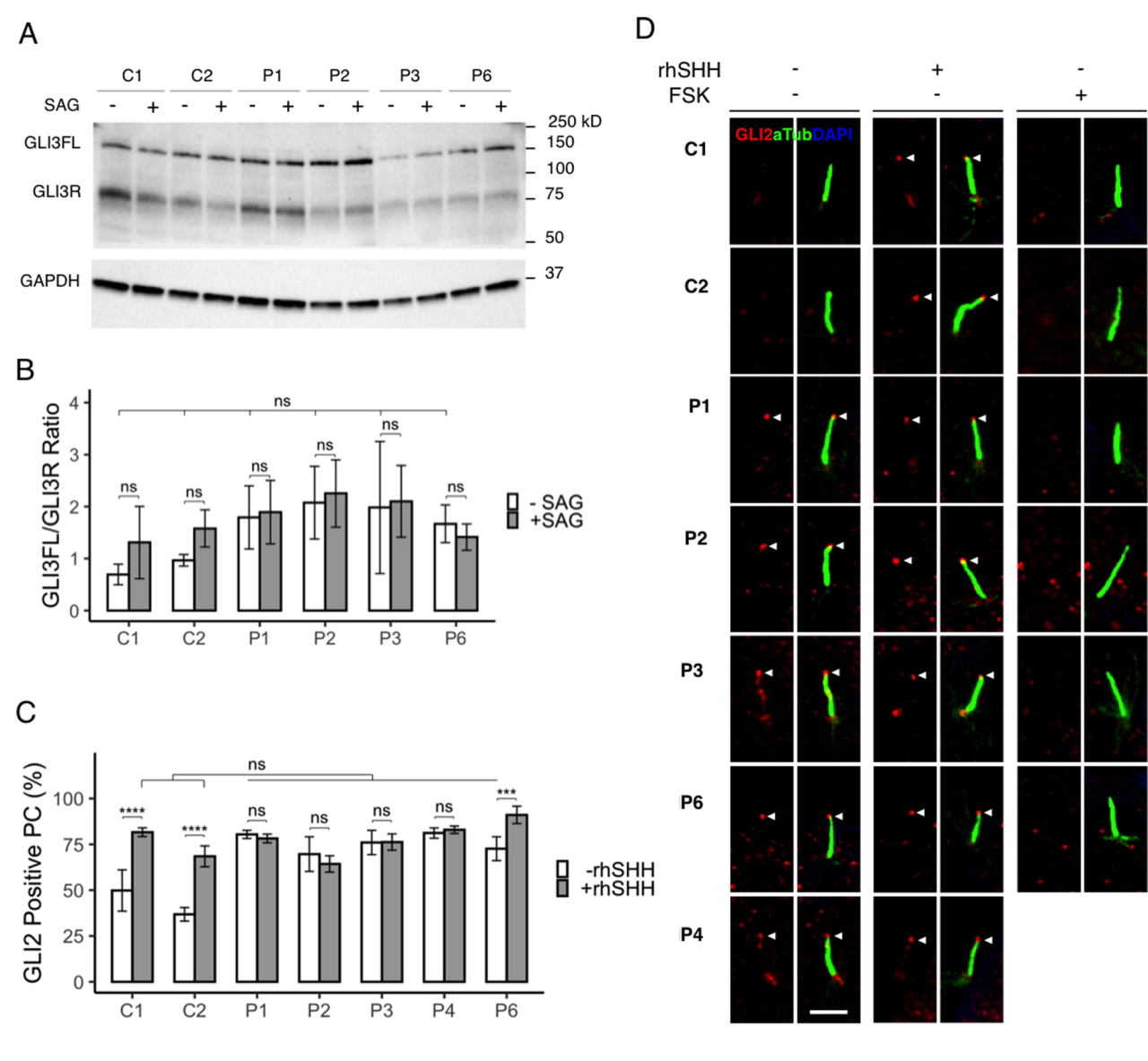
Table 2: Summary of identified *SMO* variations


P1
A1
A2
A3
A4
P2
B1
B2
B3
B4
P3
C1
C2
C3
C4
P5
E1
E2
E3
E4
E5
E6
DEBOUT
P4
D1
D2
D3
D4
D5
D6
D7
D8
P6
F1
F2
F3
P7
G1
G2
G3
G4


Family F1
I
II
T/C
G/G
C/C
G/T
T/C
G/T
P1
Chr7 g.128848674C>T;
c.781C>T; p.Arg261Cys
Chr7 g.128845484G>T;
c.1339G>T; p.Glu447*
Family F2
delAG/+
delEx1/+
delAG/+
delEx1/+
P2
delAG/+
delEx1/+
P3
Chr7 g.128852219_
128852220delAG;
c.2291_2292delAG;
p.Gln764Argfs*52
Del Exon 1
Family F3
F=1/16
A/T
A/T
T/T
P4
Chr7 g.128848620A>T;
c.1285A>T; p.Ile429Phe
Family F4
T/C
G/G
C/C
G/A
T/C
G/A
P5
Chr7 g.128850879C>T;
c.1726C>T; p.Arg576Trp
Chr7 g.128850880G>A;
c.1727G>A; p.Arg576Gln
Family F5
F=1/16
C/T
C/T
C/T
T/T
P6
T/T
P7
Chr7 g.128850879C>T;
c.1726C>T; p.Arg576Trp
AluSx
AluSz
TSPAN33
Ex1
SMO
Ex1
AHCYL2
Ex1
7q32.1: 128773868-128927701 (153Kb)


A
SMO mRNA Level
1.5
1.0
0.5
0.0
ns
***
****
**
****
ns
ns
C1 C2 P1 P2 P3 P4 P6 P7
B
F1-II:1 (P1)
c.781C>T; p.Arg261Cys
F1-II:1 (P1)
c.1339G>T; p.Glu447*
F2-II:1,2 (P2, P3)
c.2291_2292delAG;
p.Gln764Argfs*52
F5-II:2,3 (P6, P7)
c.1726C>T; p.Arg576Trp
F3-II:1 (P4)
c.1285A>T;
p.Ile429Phe
Ctrl
Exon 6
Exon 7
Cryptic splice site
C
CRD
N-Ter
Extracellular
Membrane
Intracellular
ICL2
Arg261
ICL1
Ile429
Glu447
H8
Arg576
ICL3
Gln764
C-Ter
hSMO 764 QGLG----------PIHSRTNLMDTELMDADSDF 787
mSmo 770 QGLG----------SIHSRTNLMEAEILDADSDF 793
zSmo 785 MDVGRTAVVPRADGRRGVQIHSRTNLMDAELLDADSDF 822
xSmo 779 MDLTSYSGRTQARRAGIPPMHSRANLMDAELMDTDSDF 816
D
Arg261
ICL1
Ile429
ICL2
ICL3
Gαi-α5
E
Arg261
Gαi-α5
F
3.315Å
Arg261
Tyr262
3.455Å
Cys261
Tyr262


A
aTubPCNTDAPI
C1
C2
P1
P2
P3
P4
P6
B
Ciliated Cell (%)
ns
C1 C2 P1 P2 P3 P4 P6
C
Ciliary Length (µm)
ns
C1 C2 P1 P2 P3 P4 P6
D
PTCH Induction (fold change)
+rhSHH
+SAG
****
ns
C1 C2 P1 P2 P3 P4 P6 P7
GLI1 Induction (fold change)
+rhSHH
+SAG
****
ns
C1 C2 P1 P2 P3 P4 P6 P7
F
SMO Positive PC (%)
****
C1 C2 P1 P2 P3 P4 P6
E
- rhSHH
+ rhSHH
SMOPCNTDAPI
C1
C2
P1
P2
P3
P4
P6


A
C1
C2
P1
P2
P3
P6
SAG
GLI3FL
GLI3R
GAPDH
250 kD
150
100
75
50
37
B
GLI3FL/GLI3R Ratio
ns
- SAG
+SAG
C
GLI2 Positive PC (%)
****
***
-rhSHH
+rhSHH
P4
D
rhSHH
FSK
GLI2aTubDAPI